

Renormalization for Initialization of Rolling Shutter Visual-Inertial Odometry

Branislav Micusik · Georgios Evangelidis

arXiv:2008.06399v2 [cs.CV] 24 Mar 2021

Abstract In this paper we deal with the initialization problem of a visual-inertial odometry system with rolling shutter cameras. Initialization is a prerequisite for using inertial signals and fusing them with visual data. We propose a novel statistical solution to the initialization problem on visual and inertial data simultaneously, by casting it into the renormalization scheme of Kanatani. The renormalization is an optimization scheme which intends to reduce the inherent statistical bias of common linear systems. We derive and present the necessary steps and methodology specific to the initialization problem. Extensive evaluations on ground truth exhibit superior performance and a gain in accuracy of up to 20% over the originally proposed Least Squares solution. The renormalization performs similarly to the optimal Maximum Likelihood estimate, despite arriving at the solution by different means. With this paper we are adding to the set of Computer Vision problems which can be cast into the renormalization scheme.

Keywords Visual-Inertial Odometry Initialization · Renormalization · Rolling-Shutter camera

1 Introduction

Real time pose estimation of a moving camera has been an active topic in Computer Vision and Robotics community for decades, but with the advent of Augmented Reality, the topic experiences a new hype. Augmented Reality draws new requirements on pose estimation performance as on the energy consumption side as well as on the accuracy and robustness. Mobile phones, wearable smart glasses or watches use in-built rigs with a

Snap Inc.

Fleischmarkt 3-5, 1010 Vienna, Austria, E-mail: brano@snap.com, georgios@snap.com

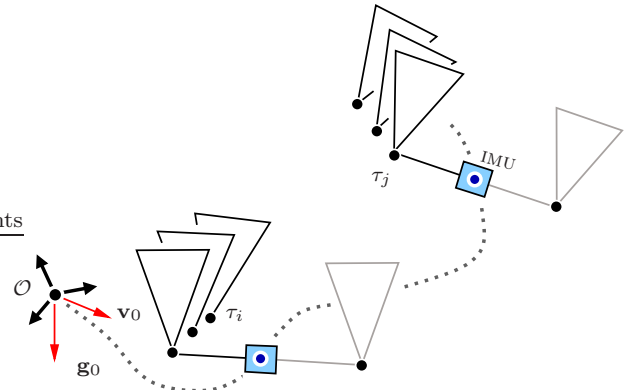


Fig. 1 Rolling shutter (stereo) camera with IMU rig in motion. This paper deals with the simultaneous estimation of the unknown initial velocity \mathbf{v}_0 and the gravity \mathbf{g}_0 from the IMU and camera data streams.

mono or stereo camera and an IMU as a de facto standard hardware. This stems from the fact that combining the two sensor modalities, the visual and inertial one, has been proven to be an ultimate solution towards compensating each others drawbacks. Common development toolkits natively support fusion of both sensors, *e.g.* ARCore (Google (2018)) and ARKit (Apple (2015)).

There are two important practical challenges to be considered. First, cameras in mobile devices are in majority rolling shutter cameras. These are cheaper and possess higher dynamic range than standard global shutter cameras. Majority of research has been, however, devoted to the standard global shutter camera models. Rolling shutter geometry has started catching the attention with the rise of mobile phones and smart glasses (Albl et al (2015); Albl et al (2016); Dai et al (2016); Hedborg et al (2012); Meingast et al (2005)). Second, IMU sensors do measure linear acceleration and angular velocity which are the second and the first derivatives

of the desired position and orientation, respectively. In order to estimate the position of an IMU over time, the integration of both signals needs to be performed. Such an integration requires knowing the initial conditions, *i.e.* the initial velocity and gravity direction. However, the IMU data alone is insufficient to estimate these initial conditions. For instance, the IMU delivers zero inertial acceleration signal when it is either static or moving with constant velocity. Without proper initial conditions, the integration leads to the same static pose. The remedy lies in fusion of the inertial with visual data as the visual cues clearly distinguish these two cases.

Yet, most systems assume that the mobile device is static at the beginning of its operation and as such, the initial velocity can be set to zero and the initial gravity direction can be deduced from the accelerometer. While this assumption may be safe in many situations, it is violated when triggering the start of a Visual-Inertial Odometry (VIO) system under motion, *e.g.* when walking or bicycling.

1.1 Contribution

In this paper we aim at estimating the initial velocity and gravity direction of a moving rig, equipped with rolling shutter cameras and an IMU, as depicted in Fig. 1. We consolidate the closed-form minimal solver of Martinelli (2013) for a general case with multiple rolling shutter cameras and partial tracks. As the main contribution, we introduce a more accurate solution by casting the original formulation into the renormalization scheme of Kanatani (1996). Namely, we reduce the problem of the original solver by Shur complement based elimination and present noise propagation analysis on the reduced problem in order to arrive at the renormalization scheme.

The renormalization scheme of Kanatani is a statistical method for certain type of problems. We show that the initialization problem can be brought by the proposed operations into the renormalization scheme. The proposed solution has superior performance to the least squares solver of Martinelli (2013) while both defined on top of the same linear system. The renormalization scheme performs comparably and sometimes outperforms the optimal Maximum Likelihood (ML) estimator which minimizes the re-projection error. Compared to the least squares, the renormalization scheme removes its inherent bias, and explicitly provides the covariance of the estimate. The renormalization scheme may suffice to solve the problem in most cases, however, it can initialize ML to enforce faster convergence.

It is known that ML entails statistical bias in the presence of what is known as “nuisance parameters”.

Various studies exist for analyzing and removing bias in the ML solution, *e.g.* by Okatani and Deguchi (2009). An optimal ML solution is usually given by a nonlinear optimization which is time-consuming when solved by numerical search. It often requires extra nuisance parameters, initial values and solving iteratively large, although sparse, linear systems. On the contrary, the renormalization procedure requires neither a priori knowledge of the initial values nor the noise level which is estimated a posteriori as a result of the renormalization itself. It consists of iterated computations of eigenvalues and eigenvectors of small matrices and bias-correction steps.

This paper adds a new problem into the set of Computer Vision problems which can be cast into the renormalization scheme. Kanatani et al (2016) formalized the renormalization scheme for many geometric computations in computer vision, *e.g.* ellipse, homography, fundamental matrix fitting, triangulation, and 3D reconstruction. These techniques show superior performance under some circumstances on many problems to the Gold Standard Methods of Hartley and Zisserman (2004) and are viable alternatives in many practical use cases.

The paper is structured as follows. First, the related work for VIO initialization and structure from motion systems as well as positioning the renormalization scheme is reviewed in Sec. 2. Then, the main concept is presented in Sec. 3. Its main parts include geometric relation of a camera and an IMU in Sec. 3.1; rolling shutter image formation in Sec. 3.2; the closed-form minimal and overconstrained solver, adjusted for rolling shutter cameras and partial feature tracks in Sec. 3.3; its reduced form in Sec. 3.4, cast as the renormalization scheme outlined and applied in Sec. 3.5. Bundle adjustment is shortly discussed and compared to the renormalization in Sec. 3.6. Finally, an extensive experimental evaluation is presented in Sec. 4, followed by the conclusion in Sec. 5.

2 Related Work

2.1 VIO Initialization

The most relevant paper to our method is the closed-form solution for initial velocity and gravity direction by Martinelli (2013). The method assumes a mono global shutter camera and complete tracks. They propose to relate corresponding visual observations through the camera baseline, which linearly depends on the unknown state parameters, that is, the velocity, the gravity in the IMU frame and the accelerometer bias. Each visual correspondence contributes three linear equations, while

the distances between map points and the cameras become unknown parameters too. The resulting linear system is solved with the constraint on the gravity magnitude. The robustness of the method against biased IMU readings was investigated by Kaiser et al (2017) and, to account for the gyroscope bias, a non-linear refinement method was proposed. Campos et al (2019) then built on Martinelli (2013) and Kaiser et al (2017), and improved the method via multiple loops of visual-inertial bundle adjustments and consensus tests. Our solution improves the least square solution and could be directly used for the bundle adjustment initialization of Campos et al (2019) or Mur-Artal and Tardós (2017). The proposed methodology could also be applied to the reduced linear solver for initial velocity and gravity direction by Evangelidis and Micusik (2021).

The above methods adopt an early fusion approach, *i.e.* a tightly-coupled fusion. Instead, the visual SfM problem can be first solved and the IMU data can be later integrated in a more loosely-coupled framework of Huang et al (2020); Kneip et al (2011); Mur-Artal and Tardós (2017). In this context, Kneip et al (2011) suggested using visual SfM to obtain camera velocity differences which are then combined with integrated IMU data to recover the scale and gravity direction. The initialization part of Mur-Artal and Tardós (2017) used scaleless poses from ORB-SLAM of Mur-Artal et al (2015) and then solved several sub-problems to initialize the state and the biases along with the absolute scale. This multi-step solution for the parameter initialization was then adapted in Qin and Shen (2017).

The initialization problem becomes harder when the device is uncalibrated (Dong-Si and Mourikis (2012); Huang et al (2020)). Even if the biases are known or ignored, the unknown orientation between the camera and the IMU makes the model non-linear and iterative optimization is necessary. Dong-Si and Mourikis (2012) propose two solutions to estimate the unknown orientation, thus allowing solving a linear system which, in turn, initializes a non-linear estimator. Instead, Huang et al (2020) builds on the multi-step approach of Mur-Artal and Tardós (2017) to jointly calibrate the extrinsics and initialize the state parameters. In a real scenario, however, the joint solution of calibration and initialization problem using only the very first few frames might make the pose tracking algorithm prone to diverge.

It is worth noting that all the above works assume that visual observations come from a global-shutter sensor. Consumer devices, however, are mostly equipped with rolling shutter cameras and rolling-shutter effects need to be handled. Proper treatment of the rolling shutter camera in connection to visual-inertial odome-

try can be found in work of Bapat et al (2018); Hedborg et al (2012); Li et al (2013); Ling et al (2018); Patron-Perez et al (2015); Schubert et al (2018, 2019). However, neither of the works copes with the initialization problem.

2.2 Renormalization

The renormalization of Kanatani (1996) was at first not well accepted by the computer vision community. This was due to the generally held preconception that parameter estimation should minimize some cost function. Scientists wondered what renormalization was minimizing. In this line of thought, Chojnacki et al (2001) interpreted renormalization as an approximation to ML. Optimal estimation does not necessarily imply minimizing a cost function and as such the renormalization is an effort to improve accuracy by a direct mean (Kanatani (2014)). The mathematical foundation of the optimal correction techniques of Kanatani et al (2016) is also discussed in the broader scope of photogrammetric statistical geometric computations by Förstner and Wrobel (2016). It is the non-minimization formalism based on error analysis which intuitive meaning is often difficult to grasp, as we will see in the following.

Regarding re-projection error minimization as the ultimate method, or the Gold Standard, the fact that the accuracy of ML can be improved was rather surprising (Kanatani (2008); Okatani and Deguchi (2009)). For hyperaccurate correction, however, one first needs to obtain the ML solution by an iterative method such as Fundamental Numerical Scheme (FNS) of Chojnacki et al (2000) on Sampson Error or Heteroscedastic Error-In-Variables (HEIV) method of Leedan and Meer (2000) and also estimate the noise level. However, it is possible to directly compute the corrected solution from the beginning, by modifying the FNS iterations if one adopts the non-minimization approach of geometric estimation of Kanatani (2014).

3 Concept

3.1 Geometry

A 3D point \mathbf{X}_i expressed in the local coordinate system of the IMU at time τ_i , projected into the coordinate system of the IMU at time τ_0 reads as

$$\mathbf{X}_0 = \mathbf{R}_i^0 \mathbf{X}_i + \mathbf{t}_i^0, \quad (1)$$

where \mathbf{R}_i^0 and \mathbf{t}_i^0 stand for the rotation matrix and the translation vector to perform this transformation. Let

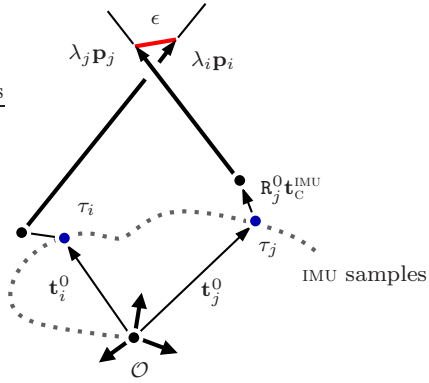


Fig. 2 Distance error ϵ being minimized by the naive least square estimator.

us assume that a camera attached to the IMU rig observes the 3D point \mathbf{X}_0 at time τ_i as

$$\lambda_i \mathbf{u}_i = \mathbf{K} (\mathbf{R}_{\text{IMU}}^{\text{C}} \mathbf{R}_0^i \mathbf{X}_0 + \mathbf{R}_{\text{IMU}}^{\text{C}} \mathbf{t}_i^0 + \mathbf{t}_{\text{IMU}}^{\text{C}}) \quad (2)$$

$$\underbrace{\lambda_i \mathbf{R}_i^0 \mathbf{R}_{\text{C}}^{\text{IMU}} \mathbf{K}^{-1} \mathbf{u}_i + \mathbf{t}_i^0 + \mathbf{R}_i^0 \mathbf{t}_{\text{C}}^{\text{IMU}}}_{\tilde{\mathbf{p}}_i} = \mathbf{X}_0$$

where $\mathbf{R}_{\text{C}}^{\text{IMU}}$, $\mathbf{t}_{\text{C}}^{\text{IMU}}$ is the known fixed relative pose from the camera to the IMU, and \mathbf{K} is the known camera calibration matrix. Image coordinates of the 3D point \mathbf{X}_0 , being tracked in multiple views, are denoted \mathbf{u}_i , and λ_i are unknown scales, the depths, of their projection rays $\mathbf{K}^{-1} \mathbf{u}_i$.

The IMU pose \mathbf{R}_i^0 , \mathbf{t}_i^0 at time τ_i is calculated as

$$\mathbf{R}_i^0 = \prod_{k=0}^{i-1} \mathbf{R}_{k+1}^k = \prod_{k=0}^{i-1} \Omega(\boldsymbol{\omega}_k \Delta\tau), \quad (3)$$

$$\mathbf{t}_i^0 = \mathbf{t}_0 + i \mathbf{v}_0 \Delta\tau + \left(\sum_{k=0}^{i-1} \beta_{k,i} \mathbf{R}_k^0 \mathbf{a}_k + i^2 \mathbf{g}_0 \right) \frac{\Delta\tau^2}{2}, \quad (4)$$

where

$$\beta_{k,i} = 2i - 2k - 1. \quad (5)$$

The 3 element vector \mathbf{a}_k and $\boldsymbol{\omega}_k$ is the accelerometer and the gyroscope readout measurements of the IMU at time τ_k , respectively. The exponential map $\Omega(\cdot)$ gives a rotation matrix from the argument vector. The time between two IMU samples is denoted by $\Delta\tau$. Without loss of generality, we set the origin into the coordinate system of the first IMU, thus the translation $\mathbf{t}_0 = \mathbf{0}$. The initial velocity \mathbf{v}_0 and the gravity vector \mathbf{g}_0 at time τ_0 , expressed in the origin, are the unknowns and subjects to estimation. For the sake of simplicity, we assume for now that the measurements are corrected for biases. The compensation of the biases is discussed later in Sec. 3.7. The biases may vary over time, and can be included in a final non-linear refinement step. We further

assume that the IMU and the cameras are temporarily synchronized.

It is to be noted that unless \mathbf{v}_0 and \mathbf{g}_0 are known, the IMU data cannot be integrated in order to get IMU poses in the above chosen origin. Most visual-inertial systems assume that the camera-IMU rig is *static* at start and it can be assumed that the initial velocity $\mathbf{v}_0 = \mathbf{0}$ and the initial gravity \mathbf{g}_0 is determined from the acceleration readout. However, in many practical situations this is violated, the system is in motion at start, *e.g.* a person rides a bicycle or walks.

3.2 Rolling shutter image formation

A rolling shutter camera is, in its principle, a moving line camera. When moving along a line, it falls into a class of linear pushbroom cameras, see (Gupta and Hartley (1997)). Each scanline is read out one after the other and all of them are stacked into an image buffer. Note that indeed the pose of the IMU in Eq. (2) differs for each i . The readout time of a scanline of the rolling shutter camera is constant even when camera exposure varies. We can therefore safely choose $\Delta\tau = \tau_{i+1} - \tau_i$ to be exactly the readout time of one line of the camera. The IMU data can be upsampled, *e.g.* for VGA resolution from a typical sampling IMU rate of 800Hz to 47.6kHz, and integrated, called the *interpolate-then-integrate* approach. As such, for each scanline of the image, we have one pose, \mathbf{R}_i^0 and \mathbf{t}_i^0 . Alternatively, the integration is performed on the original IMU sample rate and then the poses are interpolated for each scanline, the *integrate-then-interpolate* approach. We found the first approach to give slightly better results for the initialization problem. This is expected because of the non-linear dependency of translation \mathbf{t}_i^0 on gyroscope readout $\boldsymbol{\omega}_k$ in Eq. (4) and Eq. (3). Upsampling the signals first and then integrating through a non-linearity is typically recommended.

3.3 Linear Solver

Let us assume that a (stereo) camera with the IMU moves and observations of some 3D points in multiple images are available. If \mathbf{u}_i and \mathbf{u}_j are the homogeneous image observations of a point \mathbf{X}_0 in two views, then we can write Eq. (2) for each point separately. By eliminating \mathbf{X}_0 we obtain

$$\lambda_i \mathbf{p}_i + \mathbf{t}_i^0 + \mathbf{R}_i^0 \mathbf{t}_{\text{C}}^{\text{IMU}} = \lambda_j \mathbf{p}_j + \mathbf{t}_j^0 + \mathbf{R}_j^0 \mathbf{t}_{\text{C}}^{\text{IMU}}, \quad (6)$$

such that the 3 element calibrated vector $\mathbf{p}_i = \mathcal{N}(\tilde{\mathbf{p}}_i) = \mathcal{N}(\mathbf{R}_i^0 \mathbf{R}_{\text{C}}^{\text{IMU}} \mathbf{K}^{-1} \mathbf{u}_i)$, where $\mathcal{N}(\mathbf{x})$ normalizes the vector \mathbf{x}

by its third coordinate to the homogeneous coordinates. Substituting Eq. (4) into Eq. (6) yields

$$\begin{bmatrix} \xi_{ij}\mathbf{I}_3 & \mu_{ij}\mathbf{I}_3 & \kappa_{ij} & \mathbf{p}_i & \mathbf{p}_j & \cdot & \cdots & \cdot \\ \vdots & \vdots \\ \xi_{ik}\mathbf{I}_3 & \mu_{ik}\mathbf{I}_3 & \kappa_{ik} & \mathbf{p}_i & \cdot & \mathbf{p}_k & \cdots & \cdot \\ \vdots & \vdots \\ \xi_{kl}\mathbf{I}_3 & \mu_{kl}\mathbf{I}_3 & \kappa_{kl} & \cdot & \cdot & \mathbf{p}_k & \cdots & \mathbf{p}_l \end{bmatrix} \begin{bmatrix} \mathbf{v}_0 \\ \mathbf{g}_0 \\ 1 \\ \lambda_i \\ \lambda_j \\ \lambda_k \\ \vdots \\ \lambda_l \end{bmatrix} = \mathbf{0}, \quad (7)$$

where

$$\begin{aligned} \xi_{ij} &= (i-j)\Delta\tau, \\ \mu_{ij} &= (i^2-j^2)\frac{\Delta\tau^2}{2}, \\ \kappa_{ij} &= \mathbf{R}_i^0 \mathbf{t}_c^i - \mathbf{R}_j^0 \mathbf{t}_c^j + \\ &\quad + \left(\sum_{k=0}^{i-1} \beta_{k,i} \mathbf{R}_k^0 \mathbf{a}_k - \sum_{k=0}^{j-1} \beta_{k,j} \mathbf{R}_k^0 \mathbf{a}_k \right) \frac{\Delta\tau^2}{2}. \end{aligned} \quad (8)$$

In the matrix form, the Eq. (7) can be written as

$$[\mathbf{S} \ \mathbf{P}] \mathbf{x} = \mathbf{0}, \quad (9)$$

which is a linear equation system. It can be solved, for instance, in the least squares sense. It is worth noting that the error which is minimized by the above least squares solution has a geometric meaning. It relates to the distance between 3D points which are obtained through $\lambda_i \mathbf{p}_i$, as shown in Fig. 2. We tried to formulate the initialization problem on the angular error on projective rays instead of the distance. The angular error is often used in standard epipolar geometry solvers (Hartley and Zisserman (2004)), and also has been used in the relative pose for the rolling shutter camera in Dai et al (2016). For static or slow motion the error degenerates as is too sensitive to image noise. Overall, the angular error is inferior to the presented distance based error.

Each matching pair of image points adds three equations which constrain the shared unknown initial velocity and gravity (fixed six unknowns), but adds additional unknown λ 's per ray (always two new unknowns). Provided that a single point is tracked in all views, then each new image observation adds only one λ_i , and the minimum number of frames is 5 (4 pairs). The unknown λ 's are shared between multiple views as shown in Eq. (7), if a ray is used in multiple pairs. There, for the (i, j) and (i, k) pairs, λ_i is shared as the corresponding 3D point is projected into three views. This explicit sharing of λ 's better constrains the system and reduces the growth of unknowns. Similar derivations to Eq. (7) for the global shutter camera can be found in Martinelli (2013).

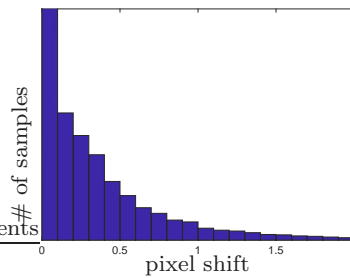


Fig. 3 Half-normal distribution of the positional error of detected FAST corners of Rosten et al (2010) and ECC tracked feature points by Evangelidis and Psarakis (2008). The error is defined as the distance between a feature point and its ground truth location on a synthetically rendered sequence with no additionally added image noise. It can be seen that it obeys Gaussian distribution under a perfect image formation model. For real images we silently assume similar behavior.

3.4 Reduced Linear Solver

We propose to eliminate the unknown λ 's from Eq. (9). This can be done with the Schur complement based elimination of the P matrix in Eq. (9) such that it becomes

$$[\mathbf{S} - \underbrace{\mathbf{P}(\mathbf{P}^\top \mathbf{P})^{-1} \mathbf{P}^\top}_{\mathbf{G}}] \mathbf{y} = \mathbf{0}, \quad (10)$$

$$[(\mathbf{I}_3 - \mathbf{G}) \mathbf{S}] \mathbf{y} = \mathbf{0}, \quad (11)$$

$$\mathbf{B} \begin{bmatrix} \mathbf{v}_0 \\ \mathbf{g}_0 \\ 1 \end{bmatrix} = \mathbf{0}, \quad (12)$$

where the matrix $\mathbf{B} = (\mathbf{I}_3 - \mathbf{G}) \mathbf{S}$ is $3N \times 7$, N is the number of pairs of point matches and $\mathbf{y} = [\mathbf{v}_0^\top \ \mathbf{g}_0^\top \ 1]^\top$ is the unknown 7 element vector. The matrix \mathbf{G} is an idempotent $N \times N$ projection matrix. Solving the reduced linear problem in Eq. (12) in the least square sense, yields the same result as Eq. (7). Depending on the sparsity of the matrix P, one or another can be faster, and should be chosen accordingly for specific practical conditions.

The reduced form simplifies the noise analysis in order to arrive to the solver presented in the next. The advantage of the reduced form in Eq. (12) is that the unknown solution vector is of *fixed* size. It contains the initial velocity and gravity only, and no longer the depth multipliers λ 's.

At the first look, it might look as if the rolling shutter camera adds difficulties in the equations in comparison to the global shutter case. However, from the geometric point of view, the opposite can be claimed. Each camera line has a different center of projection when moving and so the rays put into the triangulation equation constrain better the solution. On the other side, the rolling shutter effect adds image artifacts as

the long line segments may get projected as bent under a fast motion. However, as we experimentally observed, this is negligible for a feature tracker which uses a small image patch. Overall, the rolling shutter is a beneficial feature which implicitly encodes motion of the camera and makes it directly observable (Bapat et al (2018)).

Both Eq. (7) and Eq. (12) treat all the data as equally valuable and fall into the class of algebraic least squares estimators. In the next section we propose an improvement by involving a proper noise perturbation analysis to individually weight the point matches.

3.5 Renormalization Scheme

Class of problems like Eq. (12), where a geometric relationship in high dimensions, expressed as an implicit equation, is fitted, is called *geometric fitting* and has been studied by Kanatani (1996). The matrix \mathbf{B} in Eq. (12) is filled from the IMU sensor data and from the image point correspondences over multiple views $\mathbf{u}_{\{i,j,\dots\}}$ via their projective rays $\mathbf{p}_{\{i,j,\dots\}}$. We consider short integration time in which the effect of noise on the IMU data is negligible to the noise on the point correspondences. We experimentally verified very little accuracy gain when considering noise in the IMU data. Therefore, in the next we perform noise perturbation analysis when considering noise purely on the point correspondences.

Each image point correspondence pair $\mathbf{u}_i \leftrightarrow \mathbf{u}_j$ in Eq. (12) contributes three equations to the matrix \mathbf{B} and can be written as

$$(\mathbf{b}^{(s)}(\mathbf{u}_i, \mathbf{u}_j), \mathbf{y}) = 0, \quad s = 1 \dots 3,$$

where $\mathbf{b}^{(s)}(\cdot, \cdot)$ is one row of the matrix \mathbf{B} and $(\mathbf{a}, \mathbf{b}) = \mathbf{a}^\top \mathbf{b}$ stands for the inner product. The three equations are linearly dependent, so we see the same as in Eq. (9) that 6 is the minimal number of point correspondences to guarantee $\text{rank}(\mathbf{B}) = 6$.

The coordinates of the image point correspondences $\mathbf{u}_i, \mathbf{u}_j$ are not perfect. This is caused by the image operations, specifically the feature detection and patch based tracking on noisy image data signal. We model this uncertainty in statistical means. We assume that the observed image point \mathbf{u}_i stems from perturbation of the true value $\bar{\mathbf{u}}_i$ by independent random Gaussian variable $\Delta \mathbf{u}_i$ of zero-mean and with the covariance matrix $\mathbf{V}[\mathbf{u}_i]$, such that

$$\mathbf{u}_i = \bar{\mathbf{u}}_i + \Delta \mathbf{u}_i.$$

We experimentally validated that Gaussian noise is a feasible assumption in practical situations with an off-the-shelf feature detector and a feature tracker, see Fig. 3

for more details. We assume a 2×2 covariance matrix, known up to noise level σ ,

$$\mathbf{V}[\mathbf{u}_i] = \sigma^2 \mathbf{V}_0[\mathbf{u}_i], \quad (13)$$

where the known normalized covariance matrix $\mathbf{V}_0[\mathbf{u}_i]$ describes the orientation dependence of uncertainty in relative terms. The covariance matrix can come from uncertainty of the employed feature detector and the tracker. In all our experiments we assume $\mathbf{V}_0[\mathbf{u}_i]$ be the identity matrix.

If the observations $\mathbf{u}_i, \mathbf{u}_j$ are regarded as random variables, their nonlinear mapping $\mathbf{b}^{(s)}(\mathbf{u}_i, \mathbf{u}_j)$, which we write $\mathbf{b}_{ij}^{(s)}$, or $\mathbf{b}_\alpha^{(s)}$ for short, is also a random variable. The linear index α steps over the row triplets in the matrix \mathbf{B} in Eq. (12). Each α represents a frame pair ij and we use them exchangeably. Missing superscript in \mathbf{b}_{ij} means all three rows, *i.e.* a 3×7 matrix. Its covariance matrix is

$$\mathbf{V}^{(st)}[\mathbf{b}_{ij}] = \sigma^2 \mathbf{V}_0^{(st)}[\mathbf{b}_{ij}], \quad (14)$$

where $s, t = 1 \dots 3$ to combine mutually the rows of the three equations per correspondence, yielding nine matrices per each ij combination (or α). The covariance matrix is evaluated to first approximation in terms of the Jacobians $\mathbf{J}^{(s)}$ and $\mathbf{J}^{(t)}$ of the mapping \mathbf{b}_{ij} as follows

$$\mathbf{V}_0^{(st)}[\mathbf{b}_{ij}]_{7 \times 7} = \mathbf{J}_{ij}^{(s)} \begin{bmatrix} \sigma^2 \mathbf{V}_0[\mathbf{u}_i] & 0 \\ 0 & \sigma^2 \mathbf{V}_0[\mathbf{u}_j] \end{bmatrix}_{4 \times 4} \mathbf{J}_{ij}^{(t)\top}. \quad (15)$$

If the noise in the \mathbf{u} -space is assumed Gaussian, the corresponding noise in the transformed \mathbf{b} -space is no longer Gaussian. However, our numerical experiments have shown that in the noise range of typical feature detector and tracker, *i.e.* $\sigma \in [0, 0.5]$ pixels, such an assumption is feasible. In order to stay in the safe range, removal of systematic error like outliers prior to estimation is crucial. Correction for higher order noise terms can be omitted, as we observed that the Hyper-renormalization of Kanatani et al (2016) brings only small accuracy gain for the increased computational burden.

3.5.1 Solver

The standard Least Squares (LS) solution to Eq. (12)

$$\epsilon^2 = \frac{1}{N} \sum_{\alpha=1}^N \sum_{s,t=1}^3 (\mathbf{b}_\alpha^{(s)}, \mathbf{y})(\mathbf{b}_\alpha^{(t)}, \mathbf{y}) \quad (16)$$

$$= \left(\mathbf{y}, \left(\frac{1}{N} \sum_{\alpha=1}^N \sum_{s,t=1}^3 \mathbf{b}_\alpha^{(s)} \mathbf{b}_\alpha^{(t)\top} \right) \mathbf{y} \right) = (\mathbf{y}, \mathbf{M}_{\text{LS}} \mathbf{y}) \quad (17)$$

minimizes the mean square error ϵ^2 . Fig. 2 depicts the geometric meaning of the error. The solution can be obtained as an eigenvalue fit of the 7×7 matrix \mathbf{M}_{LS} of

$$\mathbf{M}_{\text{LS}} \mathbf{y} = \lambda \mathbf{y}.$$

Weighting each pair i, j differently, LS would turn, for small accuracy gain, into iterative re-weighted LS. More importantly, both can be fairly improved by Taubin (1991), as modification of LS and even slightly more by Kanatani (2008). Our experiments validate what has been demonstrated in the ellipse fitting problem by Kanatani (2008), that the error on the estimated entities can be sorted as naïve LS $>$ weighted LS \gg Taubin $>$ renormalization, see Sec. 4.1 and Fig. 5.

Taubin (1991) proposed to include higher noise error terms to remove the bias of LS, and such, to first order approximation of the algebraic mean square error it yields a generalized eigenvalue fit. Kanatani further improved upon this idea and proposed to iteratively re-weight the Taubin method, therefore called *renormalization* (Kanatani (1996)). In the following we present the renormalization scheme applied to the initialization of a VIO system.

Renormalization Scheme

1. Let $\mathbf{y}_0 = \mathbf{0}$ and $w_\alpha^{(st)} = \delta_{st}$, $\alpha = 1 \dots N$, $s, t = 1, 2, 3$, where δ_{st} is the Kronecker delta, equal 1 if $s = t$ and 0 otherwise.
2. Compute 7×7 matrices

$$\mathbf{M} = \frac{1}{N} \sum_{\alpha=1}^N \sum_{s,t=1}^3 w_\alpha^{(st)} \mathbf{b}_\alpha^{(s)} \mathbf{b}_\alpha^{(t)\top} \quad (18)$$

$$\mathbf{N} = \frac{1}{N} \sum_{\alpha=1}^N \sum_{s,t=1}^3 w_\alpha^{(st)} \mathbf{v}_0^{(st)} [\mathbf{b}_\alpha], \quad (19)$$

where $w_\alpha^{(st)}$ is the element of the matrix \mathbf{W}_α at the row s and column t .

3. Solve the generalized eigenvalue problem

$$\mathbf{M} \mathbf{y} = \gamma \mathbf{N} \mathbf{y} \quad (20)$$

and compute the unit eigenvector \mathbf{y} for the smallest eigenvalue γ .

4. If $\mathbf{y} \approx \mathbf{y}_0$ up to sign, continue to Step 5. Else, update

$$\mathbf{W}_\alpha \leftarrow \begin{bmatrix} (\mathbf{y}, \mathbf{v}_0^{(11)} [\mathbf{b}_\alpha] \mathbf{y}) & (\mathbf{y}, \mathbf{v}_0^{(12)} [\mathbf{b}_\alpha] \mathbf{y}) & (\mathbf{y}, \mathbf{v}_0^{(13)} [\mathbf{b}_\alpha] \mathbf{y}) \\ (\mathbf{y}, \mathbf{v}_0^{(21)} [\mathbf{b}_\alpha] \mathbf{y}) & (\mathbf{y}, \mathbf{v}_0^{(22)} [\mathbf{b}_\alpha] \mathbf{y}) & (\mathbf{y}, \mathbf{v}_0^{(23)} [\mathbf{b}_\alpha] \mathbf{y}) \\ (\mathbf{y}, \mathbf{v}_0^{(31)} [\mathbf{b}_\alpha] \mathbf{y}) & (\mathbf{y}, \mathbf{v}_0^{(32)} [\mathbf{b}_\alpha] \mathbf{y}) & (\mathbf{y}, \mathbf{v}_0^{(33)} [\mathbf{b}_\alpha] \mathbf{y}) \end{bmatrix}_{\{1,2\}}^- \quad (21)$$

$$\mathbf{y}_0 \leftarrow \mathbf{y}$$

and go back to Step 2. The expression $[\mathbf{U}]_{\{1,2\}}^-$ is the pseudoinverse with truncated rank 2 or 1. The truncation to rank 2 is done iff $\frac{\sigma_2}{\sigma_1} > 0.1$, where σ_1

and σ_2 is the first and the second largest singular value of \mathbf{U} respectively. Otherwise, the truncation to rank 1 is performed.

5. Return \mathbf{y} composed of \mathbf{v}_0 and \mathbf{g}_0 , its covariance matrix $\mathbf{V}_0[\mathbf{y}]$, and the noise level σ

$$\mathbf{V}_0[\mathbf{y}] = \frac{\sigma^2}{N} \mathbf{J}_H \mathbf{M}^{-1} \mathbf{J}_H^\top, \quad \sigma^2 = \frac{\mathbf{y}^\top \mathbf{M} \mathbf{y}}{2 - 6/N} \quad (22)$$

with \mathbf{J}_H being the Jacobian of the transformation from a homogeneous to Euclidean vector, see (Förstner and Wrobel (2016), Eq.(10.32)),

$$\mathbf{J}_H = \frac{1}{\mathbf{y}_{(7)}^2} [\mathbf{y}_{(7)} \mathbf{I}_6 \mid -\mathbf{y}_{(1:6)}].$$

Justification of estimating the noise level σ can be seen in Eq. (6.46) in Kanatani et al (2016).

The matrix \mathbf{M} determines the covariance of the final estimate of \mathbf{y} , while the matrix \mathbf{N} controls the bias of \mathbf{y} . The contribution of the renormalization scheme is the matrix \mathbf{N} . Its combination with the matrix \mathbf{M} compensates for the statistical bias which is inherent in Least Squares solution (Kanatani (2008)).

Least Squares choose \mathbf{y} which minimizes the cost function ϵ^2 in Eq. (17). In renormalization scheme there is no explicit cost function which is minimized. The estimated \mathbf{y} is obtained by solving a set of equations in order to reduce the dominant bias of optimally weighted Least Squares, such that it reaches Kanatani-Cramer-Rao lower bound (Kanatani (1996)).

The fourth step of the above algorithm deserves more attention due to switching of the pseudoinverse's truncated rank. Based on type of the problem, typically, the rank of the pseudoinverse is kept constant during the renormalization scheme. For instance, that is the case in the most similar algorithm to ours for optimal Homography estimation of Kanatani et al (2016). In that problem also three equations contribute to building the pseudoinverse of the weight matrix \mathbf{W}_α and this matrix is naturally of rank 2. This comes from the fact that only two equations out of three which go into this matrix are linearly independent. In our case, the situation is similar, but not that straightforward. The $3N \times 7$ matrix \mathbf{B} in Eq. (12) has rank 6 with many linearly dependent rows. Each row triplet which goes into the matrix \mathbf{B} is created through the elimination of lambdas in Eq. (10). How the original equations from \mathbf{S} , \mathbf{P} matrices are used for eliminating λ 's depends on the structure of the matrix \mathbf{P} and noise conditions. This drops the rank, either in most cases to 2, but occasionally to 1. When not treating the edge case of rank 1 this way, the weight matrix for the corresponding triplet may get very large weights and may cause divergence. The ratio of 0.1 was

achieved empirically in order to get good performance on all the tested sequences. We leave more rigorous theoretical understanding of this step for future work.

3.5.2 Jacobians

In order to compute the covariance matrix $V_0^{(st)}[\mathbf{b}_{ij}]$ in Eq. (15), the Jacobian matrices $J_{ij}^{(s)}$ and $J_{ij}^{(t)}$ need to be computed. Each 7×4 Jacobian matrix is factored into four matrices

$$J_{ij}^{(s)} = J_{ij}^{(s)4} J_{ij}^{(s)3} J_{ij}^{(s)2} J_{ij}^{(s)1}. \quad (23)$$

The first Jacobian captures the transformation of the point from homogeneous coordinates to the calibrated ray,

$$J_{ij}^{(s)1} = \begin{bmatrix} \frac{1}{f_i} \mathbf{I}_2 & 0 \\ 0 & \frac{1}{f_j} \mathbf{I}_2 \end{bmatrix}_{4 \times 4}, \quad (24)$$

where f_i stands for the focal length of the camera which observes \mathbf{u}_i and \mathbf{I} for the identity matrix.

The second Jacobian captures rotation of the vector. Denoting $\tilde{\mathbf{R}}_i = \mathbf{R}_i^0 \mathbf{R}_C^{\text{IMU}}$ and $\tilde{\mathbf{R}}_j = \mathbf{R}_j^0 \mathbf{R}_C^{\text{IMU}}$, then

$$J_{ij}^{(s)2} = \begin{bmatrix} \tilde{\mathbf{R}}_{i(:,1:2)} & 0 \\ 0 & \tilde{\mathbf{R}}_{j(:,1:2)} \end{bmatrix}_{6 \times 4}, \quad (25)$$

where $\tilde{\mathbf{R}}_{i(:,1:2)}$ is 3×2 matrix composed of the first two columns of the rotation matrix $\tilde{\mathbf{R}}_i$.

The third Jacobian captures the transformation to homogeneous coordinates. This would not be in general needed, however, from computational point of view, one avoids the need of derivative *w.r.t.* the \tilde{p}_z . Introducing this extra non-linearity is in practice not affecting the solution. Considering $\tilde{\mathbf{p}}_i = \mathbf{R}_i^0 \mathbf{R}_C^{\text{IMU}} \mathbf{K}^{-1} \mathbf{u}_i$ from Eq. (2), then

$$J_{ij}^{(s)3} = \begin{bmatrix} \frac{1}{\tilde{p}_{i,z}} [\mathbf{I}_2 \mid -\mathbf{p}_{i,(1:2)}] & 0 \\ 0 & \frac{1}{\tilde{p}_{j,z}} [\mathbf{I}_2 \mid -\mathbf{p}_{j,(1:2)}] \end{bmatrix}_{4 \times 6}, \quad (26)$$

where $\tilde{\mathbf{p}}_i = [\tilde{p}_{i,x} \tilde{p}_{i,y} \tilde{p}_{i,z}]^\top$, and $\mathbf{p}_i = \mathcal{N}(\tilde{\mathbf{p}}_i) = [\mathbf{p}_{i,(1:2)}]^\top$.

The fourth Jacobian captures the Schur complement based elimination of Eq. (12),

$$J_{ij}^{(s)4} = \begin{bmatrix} \frac{\partial \mathbf{b}_{ij}^{(s)}}{\partial p_{i,x}} & \frac{\partial \mathbf{b}_{ij}^{(s)}}{\partial p_{i,y}} & \frac{\partial \mathbf{b}_{ij}^{(s)}}{\partial p_{j,x}} & \frac{\partial \mathbf{b}_{ij}^{(s)}}{\partial p_{j,y}} \end{bmatrix}_{7 \times 4}. \quad (27)$$

The second dimension of four is due to the trick with homogeneous coordinates in Eq. (26), otherwise, it would be six. It brings an important saving as computing this Jacobian is computationally the most demanding part of the whole algorithm. This Jacobian requires to access the whole matrix \mathbf{B} . Let us further investigate the partial derivative *w.r.t.* to the first component $p_{i,x}$

$$\frac{\partial \mathbf{B}}{\partial p_{i,x}} = \frac{\partial (\mathbf{I}_3 - \mathbf{G}) \mathbf{S}}{\partial p_{i,x}} = -\frac{\partial \mathbf{G}}{\partial p_{i,x}} \mathbf{S}, \quad (28)$$

as outcome from derivative of Eq. (11). It is analogous for the rest three components. Recall that $\mathbf{G} = \mathbf{P}(\mathbf{P}^\top \mathbf{P})^{-1} \mathbf{P}^\top$. For any non-singular square matrix \mathbf{A} the following holds (Golub and van Loan (2013))

$$\frac{\partial \mathbf{A}^{-1}}{\partial \alpha} = -\mathbf{A}^{-1} \frac{\partial \mathbf{A}}{\partial \alpha} \mathbf{A}^{-1}.$$

This allows to split inversion and derivative of the matrix. It can be computed only once as it is independent on the α . Since \mathbf{G} is a regular idempotent projection matrix, then we can apply it to get

$$\frac{\partial \mathbf{G}}{\partial p_{i,x}} = \frac{\partial \mathbf{P}}{\partial p_{i,x}} \tilde{\mathbf{P}} \mathbf{P}^\top + \mathbf{P} \tilde{\mathbf{P}} \frac{\partial \mathbf{P}^\top}{\partial p_{i,x}} - \mathbf{P} \tilde{\mathbf{P}} \frac{\partial (\mathbf{P}^\top \mathbf{P})}{\partial p_{i,x}} \tilde{\mathbf{P}} \mathbf{P}^\top, \quad (29)$$

where $\tilde{\mathbf{P}} = (\mathbf{P}^\top \mathbf{P})^{-1}$. The factors $\tilde{\mathbf{P}} \mathbf{P}^\top$, $\mathbf{P} \tilde{\mathbf{P}}$ are computed only once for all the correspondences. The three partial derivatives are correspondence dependent as they depend on i and j . Since the matrix \mathbf{P} is very sparse and linear in \mathbf{p} , the derivative matrices contain only few 1's depending how often \mathbf{u}_i appears in the correspondence pairs. Overall, using factorization in Eq. (29) and sparse matrix calculus, the total Jacobian in Eq. (23) can be calculated very efficiently.

3.6 Renormalization vs. Bundle Adjustment

In order to demonstrate performance of the renormalization *w.r.t.* to the optimal Maximum Likelihood estimator, we employ the Bundle Adjustment (BA) framework. We use the solution of Eq. (11) in Eq. (7) to compute λ 's and we then average the multiple reconstructions per point to estimate the initial points \mathbf{X} . The BA algorithm minimizes the total re-projection error $\sum_i \|\mathbf{u}_i - \hat{\mathbf{u}}_i(\cdot)\|^2$, where $\hat{\mathbf{u}}_i(\cdot)$ is the resulting non-linear mapping of \mathbf{v}_0 , \mathbf{g}_0 and the auxiliary variable \mathbf{X} , while index i runs over all the observations. Note that our goal is to use a standard framework as a baseline to evaluate the performance of the proposed estimator. Therefore, we stay with the same and necessary parameters of velocity and gravity and we do not augment the set of unknowns with the sensor biases. To refine the parameters, the Levenberg-Marquardt algorithm is used, similar to the visual BA framework of Lourakis and Argyros (2005).

The renormalization, despite not being an optimal ML estimator, can in practical situations well replace BA, as will be demonstrated in Sec. 4. The accuracy of both methods is very comparable, but the computational burden differs. There are multiple advantages of the renormalization over BA, as the renormalization

- does not need auxiliary variables to be introduced as are the 3D points \mathbf{X} for BA.

- needs no initial conditions. Renormalization in its first iteration starts with the Taubin (1991) method and then iteratively renormalizes the matrices. BA needs a good starting point.
- solves in each iteration a generalized eigenvalue problem of size 7×7 which is very fast and can be solved within microseconds. BA solves iteratively a linear system of normal equations of the matrices $\sim 450 \times 450$ in case ~ 150 feature points are tracked. Despite the sparsity of the problem, the computational time is by two magnitudes higher, and goes to milliseconds.
- converges in no more than 2-5 iterations. BA needs typically at least 15 iterations.
- provides the covariance matrix of \mathbf{v}_0 and \mathbf{g}_0 explicitly without any extra computations and this is directly encoded in the matrix \mathbf{M} in Eq. (18). BA computes the covariance matrix implicitly.
- provides an estimate of the noise level on the feature points in Eq. (22). In BA, one cannot explicitly estimate the noise level.

3.7 Accelerometer and Gyroscope Bias

Recall that we assume a calibrated device and any estimated offset has been removed from the IMU data. However, a small and slowly varying bias may still be present, while it can be modeled as a constant offset owing to the short integration time. For completeness, we show how the biases can be added.

As shown in Martinelli (2013), a constant accelerometer bias can be modeled in a linear way. Such a bias can be likewise inserted into the solver of Eq. (7), that is, $\boldsymbol{\kappa}_{ij}$ can be replaced by

$$\hat{\boldsymbol{\kappa}}_{ij} = \boldsymbol{\kappa}_{ij} + \zeta_{ij} \mathbf{e}_a \quad (30)$$

where

$$\zeta_{ij} = \left(\sum_{k=0}^{i-1} \beta_{k,i} \mathbf{R}_k^0 - \sum_{k=0}^{j-1} \beta_{k,j} \mathbf{R}_k^0 \right) \frac{\Delta\tau^2}{2}, \quad (31)$$

and \mathbf{e}_a denotes the accelerometer bias. It is straightforward to show that $\zeta_{ij} \rightarrow \mu_{ij} \mathbf{I}$ when the system does not rotate. As a result, \mathbf{e}_a is not always identifiable, and separable from \mathbf{g}_0 .

Instead, $\boldsymbol{\kappa}_{ij}$, \mathbf{p}_i and \mathbf{p}_j depend on the gyroscope bias in a non-linear way. The small bias magnitude let us though use a first-order approximation, that is, $\boldsymbol{\kappa}_{ij}$ can be now replaced by

$$\hat{\boldsymbol{\kappa}}_{ij} \simeq \boldsymbol{\kappa}_{ij} + \frac{\partial \boldsymbol{\kappa}_{ij}}{\partial \mathbf{e}_\omega} \mathbf{e}_\omega \quad (32)$$

and likewise

$$\hat{\mathbf{p}}_i \simeq \mathbf{p}_i + \frac{\partial \mathbf{p}_i}{\partial \mathbf{e}_\omega} \mathbf{e}_\omega, \quad (33)$$

where \mathbf{e}_ω is the constant gyroscope bias and $\frac{\partial \boldsymbol{\kappa}_{ij}}{\partial \mathbf{e}_\omega}$, $\frac{\partial \mathbf{p}_i}{\partial \mathbf{e}_\omega}$ are the respective Jacobians. Note that the gyroscope bias directly affects the rotation, that is, biased gyroscope data is integrated in Eq. (3). In order to compute $\frac{\partial \boldsymbol{\kappa}_{ij}}{\partial \mathbf{e}_\omega}$, some useful properties of the exponential map, see (Forster et al (2017)), thus leading to the following approximations

$$\frac{\partial (\mathbf{R}_i^0 \mathbf{t}_c^i)}{\partial \mathbf{e}_\omega} \simeq -\mathbf{R}_i^0 [\mathbf{t}_c^i]_\times \frac{\partial \mathbf{R}_i^0}{\partial \mathbf{e}_\omega} \quad (34)$$

and

$$\frac{\partial \left(\sum_{k=0}^{i-1} \beta_{k,i} \mathbf{R}_k^0 \mathbf{a}_k \right)}{\partial \mathbf{e}_\omega} \simeq - \sum_{k=0}^{i-1} \beta_{k,i} \mathbf{R}_k^0 [\mathbf{a}_k]_\times \frac{\partial \mathbf{R}_k^0}{\partial \mathbf{e}_\omega}, \quad (35)$$

where

$$\frac{\partial \mathbf{R}_i^0}{\partial \mathbf{e}_\omega} \simeq \sum_{k=0}^{i-1} \mathbf{R}_{k+1}^i \mathbf{J}_k \Delta\tau \quad (36)$$

with \mathbf{J}_k being the *right* Jacobian of SO3 at $\boldsymbol{\omega}_k$ (see Eq.(8) in Forster et al (2017)). The notation $[\cdot]_\times$ denotes the skew symmetric matrix. Based on Eq. (34), the Jacobian $\frac{\partial \mathbf{p}_i}{\partial \mathbf{e}_\omega}$ can be computed by

$$\frac{\partial \mathbf{p}_i}{\partial \mathbf{e}_\omega} \simeq -\mathbf{J}_N \mathbf{R}_i^0 [\mathbf{R}_c^{\text{IMU}} \mathbf{K}^{-1} \mathbf{u}_i]_\times \frac{\partial \mathbf{R}_i^0}{\partial \mathbf{e}_\omega}, \quad (37)$$

where \mathbf{J}_N is the Jacobian of the transformation $\mathcal{N}(\mathbf{x})$ and is given by the first block of $\mathbf{J}_{ij}^{(s3)}$ in Eq. (26).

When both the biases need to be modeled, Eq. (30) can be combined with Eq. (32), while the cross dependence of biases can be ignored.

Adding biases into the renormalization scheme by involving the above equations is rather straightforward. In short, in case of the accelerometer bias, the matrix \mathbf{S} in Eq. (7) would contain three additional columns before the last column of $\boldsymbol{\kappa}$'s. The solution vector \mathbf{x} would contain the unknown \mathbf{e}_a . As entries into these columns do not depend on \mathbf{u}_i , nothing substantial changes. In case of the gyroscope bias, three extra columns would be again added into the matrix \mathbf{S} and the unknown \mathbf{e}_ω into the solution vector \mathbf{x} . The entries into \mathbf{S} now depend on \mathbf{u}_i , see Eq. (33), so the matrix \mathbf{B} in Eq. (12) has different form. Its partial derivative in Eq. (28) needs to take into account the derivative of the matrix \mathbf{S} as well. The Jacobian in Eq. (23) changes to size 10×4 . If both biases are considered, the size of the Jacobian is 13×4 .

Kaiser et al (2017) tested the robustness of Martinelli (2013) against biased IMU readings. As far as

the accelerometer bias is concerned, when it is identifiable, the initialization remains unaffected. In particular, their experiments show that even large unrealistic bias magnitudes can be well compensated. Therefore, we only expect a minor refinement through the renormalization scheme.

On the contrary, the initializer may be affected from a gyroscope bias when its magnitude is relatively large and the integration time is long (Kaiser et al (2017)). However, the rolling-shutter camera allows short integration times and the initializer would not benefit much from modeling a gyroscope bias of low magnitude. As such, it is advised to leave estimation of the biases for the followed VIO system which considers much longer temporal window allowing to model their distributions more properly.

4 Experiments

The proposed modeling is valid with either a monocular or a multiocular sensor. What is different though is the integration time needed to reliably initialize the state, because the reliability grows with the number of images. The stereo baseline leads to larger camera displacements, which in turn leads to better visual constraint via triangulation. For instance, given two successive stereo frames, the displacement from the current left to the next left camera is most of the times smaller than the distance between the current left and the next right camera. Considering more frames or widening their baseline means increasing integration time of IMU signals. This in general would be preferable, however, it means gathering more noise and making IMU contribution less trustworthy. A stereo setup allows for a good trade-off, to utilize visual information even when the camera displacement is small and the integration time of IMU signals is short. The stereo setup has significant advantage such that even in case of no motion, the stereo baseline still allows that the triangulation constraint to be effective and to correctly estimate zero velocity. We provide comparison of mono vs. stereo to support these arguments, however, we stick in our experiments to the stereo setup as being practically much more interesting and a suitable option, and a de facto gold-standard in wearable smart glasses.

4.1 Synthetic Data

In this section we perform quantitative synthetic analysis to investigate influence of noise on the final estimate of \mathbf{v}_0 and \mathbf{g}_0 . In order to get realistic data with ground truth (GT) structure and poses, we process data from

Snap Spectacles glasses with IMU BMI160. States resulting from a Kalman filter on visual-inertial data play the role of GT states and high-order splines on the IMU data provide ideal gyroscope and acceleration readings, such that a continuous integrator perfectly interpolates between the states. The IMU data are then sampled at 800Hz and finally, noise and time varying biases are added based on the calibrated variances of the used device. The device was moved forward 9m along a straight trajectory with repeatedly changing viewpoint rotation from left to right. The shape of the trajectory and velocity can be seen in Fig. 9(c). We simulate a stereo camera with a baseline of 14cm attached to the IMU. During the data acquisition, the glasses were shortly static at the beginning such that we could safely initialize the IMU state with the static motion assumption. It allows to integrate the signals to get the ground truth poses.

To produce the image correspondences, we generate 50 random feature points in the first left stereo image, assign them random depths in the range [1, 15]m and project the 3D points into the other views. We then perturb the feature points with Gaussian noise $\sigma = \{0, 0.1, \dots, 0.5\}$ pixels, the accelerometer with standard deviation of 0.005 ms^{-2} and the rotations \mathbf{R}_i^g computed from the gyroscope data with 0.02 deg at random orientation. At each σ we repeat 100 random realizations. The evaluated errors are defined as the norm on the velocity difference vector and the angle between the gravity vectors, *i.e.*

$$\begin{aligned} \epsilon_{\mathbf{v}_0} &= \|\mathbf{v}_0 - \mathbf{v}_0^{\text{GT}}\|_2, \\ \epsilon_{\mathbf{g}_0} &= \angle(\mathbf{g}_0, \mathbf{g}_0^{\text{GT}}) \end{aligned} \quad (38)$$

for one realization. We repeat the same procedure for each five-tuple of stereo images, which is slid along the whole sequence at 22 consecutive camera positions. In all the experiments, we use consecutive five stereo cameras at 10fps. This means five tuple of images in 0.5s and thus the movement of 0 - 0.3m. To show the final statistics, at each σ we compute mean and standard deviation.

Recall that the visual constraints are fed into the solver in Eq. (7) as image pairs, as shown for ij , ik , kl . Let us denote the cameras in the order: first left, first right, second left, second right and so on as $\{\text{L1}, \text{R1}\}$, $\{\text{L2}, \text{R2}\}$, $\{\text{L3}, \text{R3}\}$, $\{\text{L4}, \text{R4}\}$, $\{\text{L5}, \text{R5}\}$. Then we feed the following camera pairs into the matrix: L1 – R2, L1 – R3, L1 – R4, L1 – R5, L2 – R3, L2 – R4, L2 – R5, L3 – R4, L3 – R5, L4 – R5. We experimented with various combinations, and chose this as a trade-off between speed and accuracy. In case of a mono camera, the links would be between L cameras only.

The results can be seen in Fig. 4. We compare three methods, (i) the Least Squares of Sec. 3.3, LS, (ii) the

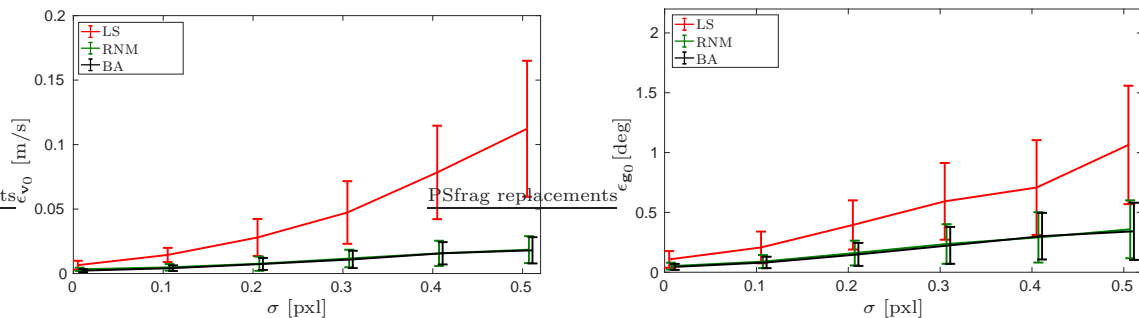


Fig. 4 Synthetic noise analysis. The vertical error bars depict the standard deviation over hundreds of realizations at the particular σ across a whole sequence. The shorter error horizontal bars on the RNM and BA are from the estimated covariances, while the longer ones are the empirical ones, computed as standard deviation on corresponding errors.

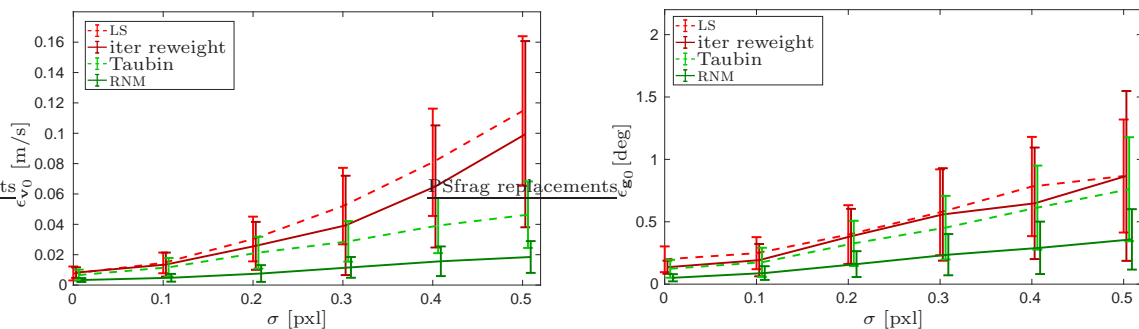


Fig. 5 Comparison of the naïve LS method, its iterative reweight modification, Taubin method, and its iterative RNM modification. See Fig. 4 for more details on axis meaning.

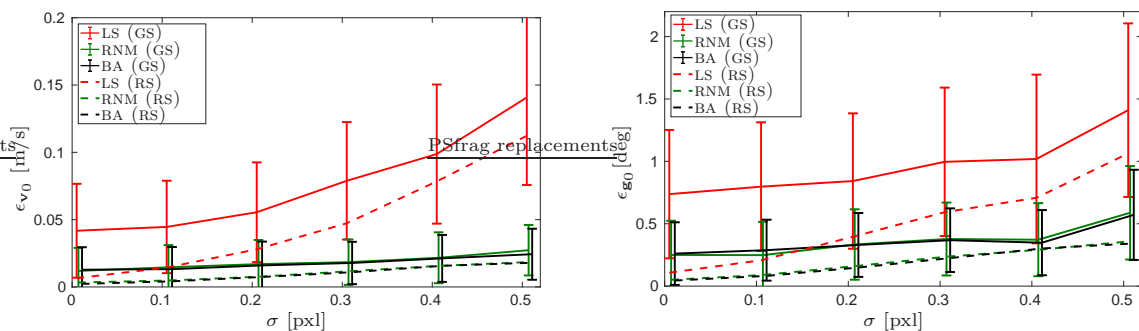


Fig. 6 Effect of Global Shutter (GS) vs. Rolling Shutter (RS) camera modeling. Solid lines show the baseline LS method of Martinelli (2013), our proposed RNM method, and the BA when GS camera model is used on RS camera data. Dashed lines represent the correct modeling from Fig. 4, review it for more details.

proposed renormalization of Sec. 3.5, RNM, (iii) Bundle Adjustment as ML with Levenberg-Marquardt, BA, detailed in Sec. 3.6, initialized by LS. Initializing BA by RNM rapidly speeds up the convergence, but does not improve the accuracy. For the two latter methods, RNM and BA, we can compute standard deviations of the estimated \mathbf{v}_0 and \mathbf{g}_0 from the theoretical covariance matrices. For RNM, see Eq. (22), for BA, see Eq. (A6.10) (Hartley and Zisserman (2004)). They both require knowing the noise level σ , see Eq. (13). To fairly compare, we set it to the ground truth σ at which the corresponding simulation is performed. However,

we confirmed that the estimated noise level σ by the renormalization in Eq. (22) is very tight to the ground truth. As can be seen, the theoretical values are very well aligned to the empirical ones and can be well utilized in practice, to know how much to trust the final estimate.

As expected, LS is by far the worst estimation, fairly improved by the renormalization, and very slightly polished by ML of BA. Moreover, renormalization returns estimate of the noise level of the feature detector / tracker. Due to perturbation with the ideal Gaussian noise, the minimization of the re-projection error is a

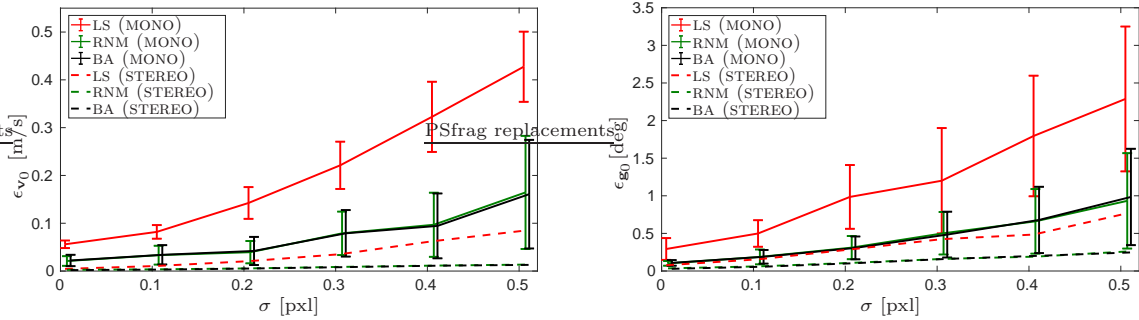


Fig. 7 Mono vs. Stereo. Solid lines show the baseline LS method of Martinelli (2013), our proposed RNM method, and the BA when monocular camera is used. Dashed lines represent the stereo camera setup from Fig. 4, review it for more details.

perfect Maximum Likelihood estimate. Using real data, this might be slightly violated and the BA is not ML in its strict sense. We will see that with the real data it may result in RNM sometimes outperforming BA.

LS variant methods. We show the performance of the proposed renormalization method in comparison to previously introduced techniques which improve the naïve LS. First, the well known iterative modification of LS (Iterative Reweight or weighted LS) is tested. The Iterative Reweight sets the matrix \mathbf{N} in Eq. (20) to identity matrix. Second, the Taubin method, where both weights $w_\alpha^{(st)}$ in Eq. (18) and Eq. (19) are dropped. Recall that the presented renormalization is its iterative modification. This experiment validates the claim of Kanatani (2008), that the error on the estimated entities can be sorted as naïve LS > weighted LS \gg Taubin > renormalization, see Fig. 5. Both LS and Taubin are both non-iterative methods which are interesting when computational resources are limited. The plots give intuition how much accuracy can be gained when running 5 iterations. Each additional iteration costs the same as the iteration of the baseline method, *i.e.* of LS for iterative reweight and of Taubin for the renormalization.

Global vs. Rolling Shutter. We show in Fig. 6 the systematic error, imposed by using Global Shutter camera model on Rolling Shutter camera imagery. GS camera is modeled such that a whole frame is assigned one single pose, the rotation and the translation of the middle row of the RS image. As already stated, we used trajectory reported in Fig. 9(c) where the average velocity is roughly 0.7 m/s. Our proposed method demonstrates superior and still a reasonable performance also in this case when the camera model does not fully explain the data. In connection to VIO systems, the fact that neglecting the RS effect in camera modeling yields drift even for moderately moving walking sequences has been shown by Li et al (2013); Patron-Perez et al (2015); Schubert et al (2018, 2019).

Mono vs. Stereo. We compare in Fig. 7 a mono to a stereo camera case with the same frame rate, that is,

the same integration time. As can be seen, the monocular case is much more sensitive to noise on the image points. Note that in common use cases a camera moves forward with epipoles being close to the image center which makes the triangulation weakly constrained. To overcome this, it would require to decrease the frame rate and thus to increase the integration time which may, however, gather too much noise. The stereo setup on the other hand keeps the visual constraint still well enforceable, independently on the motion, and provides much superior performance. Note that renormalization and BA in comparison to LS still deliver meaningful results even for the mono case, although BA needs 4 times more iterations.

More vs. Less Frames. We show in Fig. 7 comparison of more vs. less frames used for all three methods. Less frames means to still use five stereo camera frames, but considering only the pairs with the first camera only, *i.e.* L1 – R2, L1 – R3, L1 – R4, L1 – R5. For LS and RNM it means 4 frame pairs instead of 10 which yields less entries into the input matrices \mathbf{S} and \mathbf{P} in Eq. (7). For BA it means 5 observations per 3D point instead of 8. Less constraints imply lower accuracy, however, RNM and BA gain a speed-up of $3\times$ and $1.2\times$, respectively, for a small accuracy drop. Important note is that the proposed RNM does not need that many observations as LS due to the proper weighting which suppresses less confident measurements. The baseline LS needs many more observations to statistically cancel the noise instead.

Synthetic experiments presented in this section allow us to perform noise perturbation analysis and to give the reader better intuition on different configurations. We skip such detailed comparisons for real sequences, as we see analogous behavior which leads to the same conclusions. Therefore, for following qualitative as well as quantitative results on image sequences we use the best configuration, *i.e.* RS stereo with more frames.

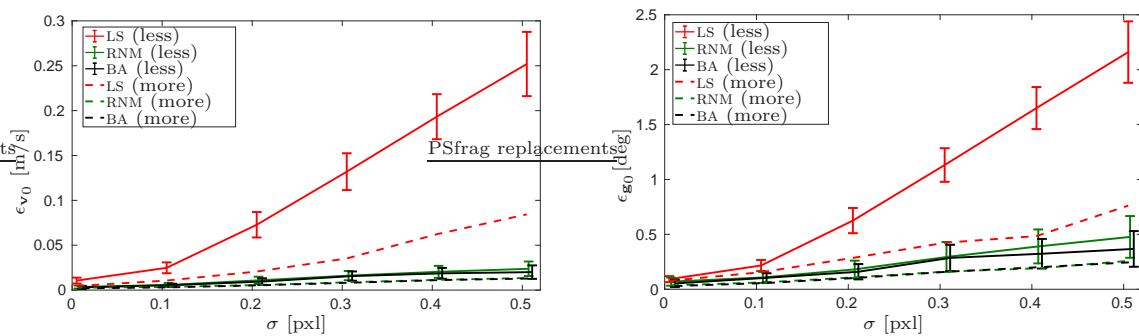


Fig. 8 More vs. Less frames. Solid lines show the baseline LS method of Martinelli (2013), our proposed RNM method with 4 pairs, and the BA when 5 frames are used. Dashed lines represent the stereo camera setup from Fig. 4 with 10 frame pairs and 8 frames, respectively.

4.2 Rendered Data

We perform qualitative comparison on realistic rendered image data, as this gives us perfect ground truth to compare to. We deploy Unreal Engine of Epic Games (2019) for rendering the images. We obtained the trajectories and the IMU data the same way as described in the previous section, for various types of walking trajectories of Snap Spectacles glasses. We simulate two virtual VGA rolling shutter cameras with noisy sensors, with the baseline of 14 cm, and readout time of 10 ms. As an input into the initializer, the IMU data is perturbed by Gaussian noise and biases on accelerometer and gyroscope with random walk noise. The features are detected by the FAST corners of Rosten et al (2010) and further tracked by the ECC tracker of Evangelidis and Psarakis (2008). In order to prune outliers we use vanilla RANSAC with the minimal solver of Sec. 3.4. To confirm the feasibility of the statistical assumption, we plot the error distribution of the tracked features which can be obtained through known depth values of the rendered images. As the Fig. 3 depicts, the distribution is Gaussian with subpixel accuracy. Based on this observation, we believe that Gaussian distribution on the image correspondences is a reasonable assumption.

We report quantitative results in Tab. 1 for the six sequences, shown in Fig. 9, Fig. 10, and Fig. 11. The "forward" trajectory is shown in Fig. 9, the "loop" trajectory in Fig. 10. The "fast shaking" trajectory is 0.5 m wide left-right shaking motion with rapid acceleration and average velocity of 0.9 ms^{-1} . The "for/back-ward" trajectory is 14 m straight forward, followed by 180° turn and back to the start with the average speed 1.8 ms^{-1} . We captured these typical motions of a person when wearing smart glasses when moving in the office space shown in Fig. 12.

We present detailed qualitative results for two sequences. The first sequence, SUBWAYTRAIN is a forward 9 m long sequence inside a static subway train,

see Fig. 9. The second sequence, TRAPCAM is a loop shaped 25 m long sequence outdoors, see Fig. 10.

The results confirm the observation from the Synthetic experiment that LS method can be improved by the renormalization RNM which is comparable and sometimes better to ML estimation of BA. In most cases, the initial velocity \mathbf{v}_0 and gravity \mathbf{g}_0 are both improved *w.r.t.* the LS, and this by roughly 20% and 8%, respectively. This is a significant improvement.

4.3 Real Data

We use real data from the Snap Spectacles glasses, as stereo images as well as IMU readings. We do not possess ground truth for these sequences. Instead, we run a typical VIO system based on the temporal Extended Kalman Filter, similar to Li et al (2013); Mourikis and Roumeliotis (2007). The filter framework fuses inertial and visual data in iterative updating procedure for maximum a posteriori probability of a linear dynamical system. The filter uses a strong prior that the sequences are static at the beginning, copes with a rolling shutter stereo camera and optimizes also for both accelerometer and gyroscope biases. For the proposed solver, though, we do not include the biases as we found that their magnitude is low in the used device.

The first is the OFFICELOOP, a loop-shaped 25 m long sequence in a typical open space office. Since there is only negligible drift between the end and starting position, we can consider the used VIO as a reasonably accurate baseline to compare to. The second WALK is a forward 36 m long sequence outdoors. Both sequences are acquired during a walk.

The results align with the previous synthetic and rendered experiments; the renormalization RNM is similar to ML estimation of BA, both outperforming the Least Squares LS. As mentioned, we do not have the ground truth and the comparison for these sequences

	SUBWAYTRAIN forward	TRAPCAM loop	STORAGEHOUSE fast shaking	STORAGEHOUSE loop	SEASIDE TOWN forward	SPACESTATION for/back-ward
LS [ms^{-1} / deg]	.015 / .125	.059 / .81.	.089 / 1.28	.027 / .47	.057 / 1.01	.065 / .38
RNM [% / %]	15 / 5	9 / 8	24 / 6	35 / 12	16 / 15	26 / 7
BA [% / %]	15 / 33	18 / 5	16 / 5	42 / 21	8 / 17	22 / 12

Table 1 Quantitative results. Each column shows the name of the sequence, type of the motion, mean of the absolute distance error on the initial velocity / mean of the angular error on the gravity to the baseline Least Squares method LS in Eq. (38). For the RNM and BA improvements in percentage are shown.

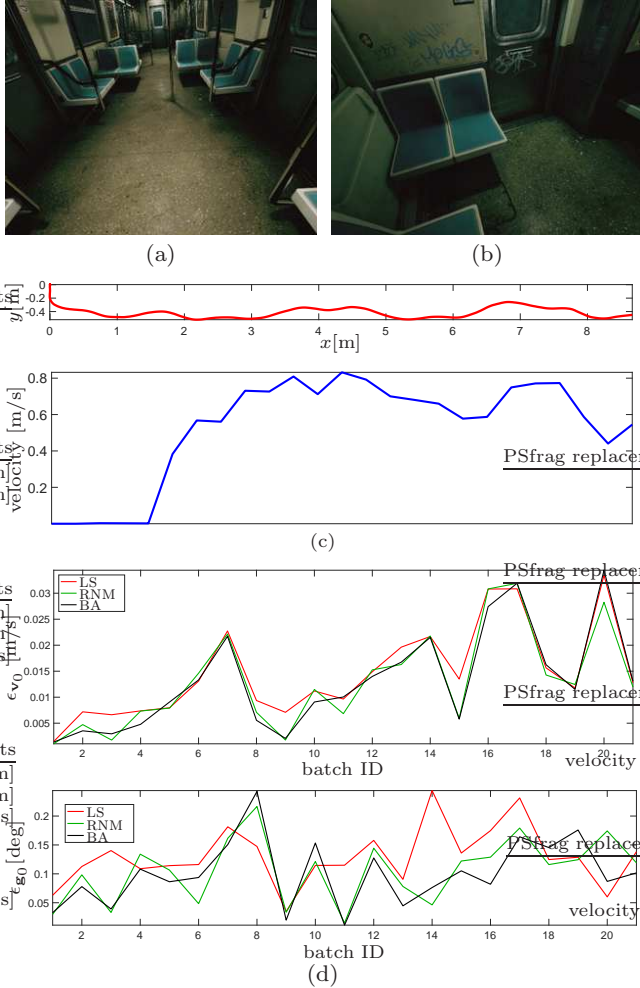


Fig. 9 SUBWAYTRAIN sequence. (a) The first and (b) the last left stereo image of the sequence. (c) Shape of the trajectory (top) and magnitude of the velocity during the motion (bottom). (d) The distance error of the estimated and the ground truth initial velocity v_0 (top). The angular error of the estimated and the ground truth gravity g_0 (bottom).

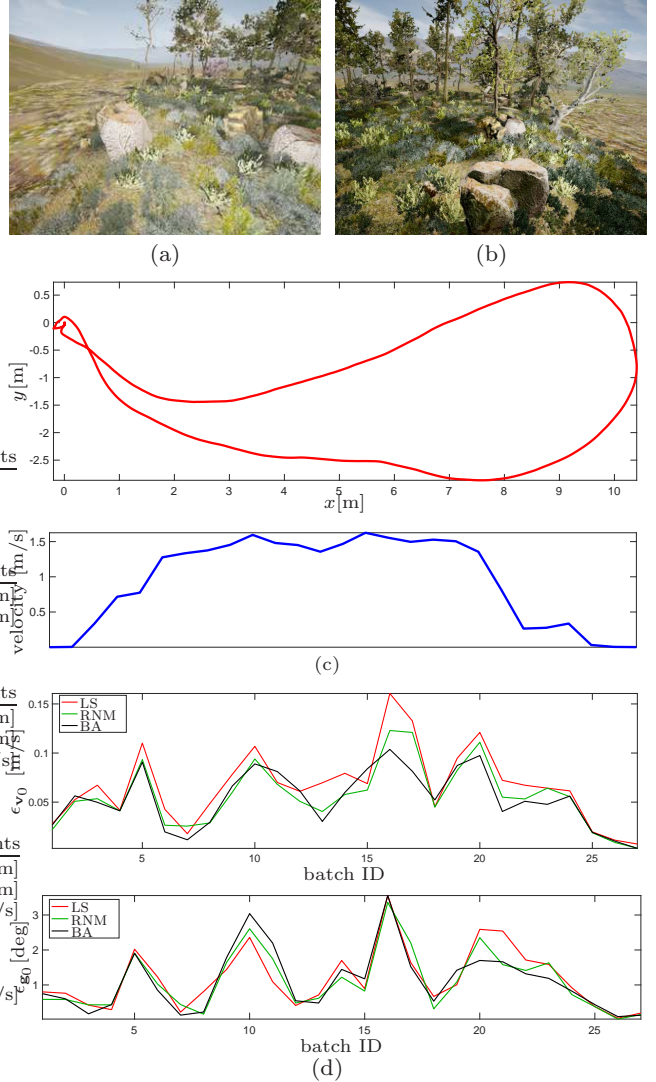


Fig. 10 TRAPCAM sequence. Left stereo image (a) at the start and (b) in the middle of the sequence. See Fig.9 for the remaining caption.

4.4 Complexity

might not be representative. What should be noticed and taken from these results is that the renormalization and ML estimator perform very similarly to each other, although, arriving to the solution by different means.

The renormalization scheme and Bundle Adjustment require different operation flow which yields different complexity. We give hints to the expected performance by pinpointing the most time consuming parts during the computations.



Fig. 11 Example images of the rendered sequences.

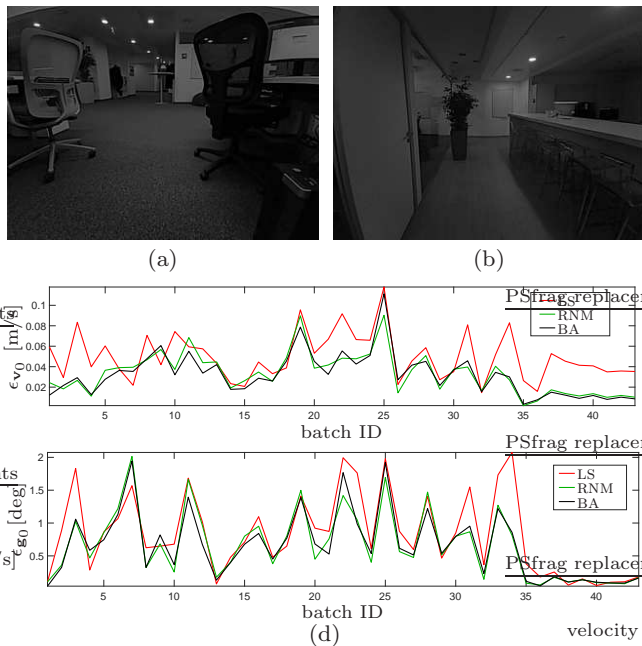


Fig. 12 OFFICELOOP sequence. Left stereo image (a) at the start and (b) in the middle of the sequence. Trajectory is the same as in Fig. 10(c). See Fig. 9 for the remaining caption.

Renormalization. Complexity of renormalization is driven by computation of the partial derivatives in Eq. (29) which is needed for the covariance matrix in Eq. (15) to fill M and N matrices. The involved matrices in Eq. (29) are sparse with derivatives of P consisting of a few ones (4 entries for a point tracked in 5 frames). Taking this into account yields many savings in computation. The generalized eigenvalue problem on 7×7 matrix itself is negligible, and typically only 3 iterations suffices.

Bundle Adjustment. Complexity in Levenberg-Marquardt optimizer is spread roughly equally into three parts. First, building a sparse linear system of normal equations with $2N \times (3M + 6)$ matrix and its corresponding right hand side vector, where N is the number of observations and M the number of auxiliary 3D points. Second, making the matrix square by left multiplying with its transpose. Third, running a sparse linear solver. Typically, 15 iterations are needed.

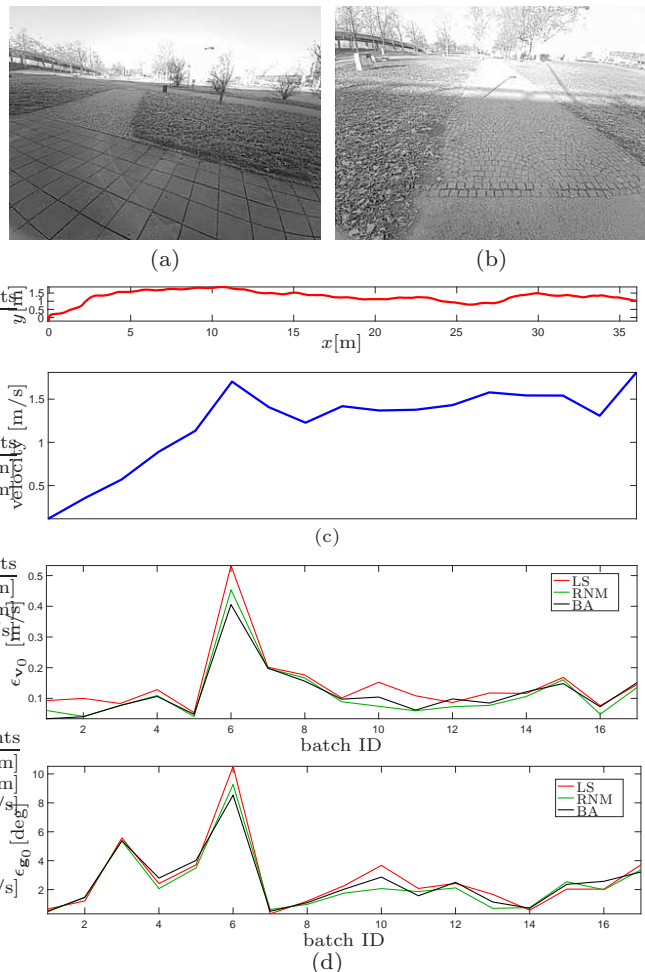


Fig. 13 WALK sequence. Left stereo image (a) at the start and (b) in the middle of the sequence. See Fig. 9 for the remaining caption.

With our MATLAB implementations, the tests on the presented rendered and real sequences show that the RNM method takes on average around 70% of the time of BA, depending on the number of considered frame pairs and length of the tracks. Our C++ implementation of the baseline LS method takes on average ~ 6 ms and of BA ~ 25 ms on an i7@2.6GHz CPU, given input inlier observations, considering five stereo frames with their pairing detailed in Sec. 4.1.

5 Conclusion

We presented a novel way to solve the initialization problem of the inertial-visual odometry system. We derived a novel solver through proper statistical modeling and we cast the problem into the renormalization scheme of Kanatani. We incorporated proper noise propagation thus yielding a solution which exhibits higher accuracy over the original Least Squares solution. The extensive evaluation shows that the renormalization scheme performs very closely to the ML estimator which is statistically optimal in case of Gaussian noise. As such, the renormalization can serve to get a very good initial point for the ML, or fully replace it, as the additional improvement is rather small for the cost of more computations.

With this paper, we add a new problem into the set of problems in Computer Vision which can be beneficially solved by the renormalization scheme. As the set of problems where the renormalization improves Gold Standards grows, the renormalization scheme is slowly finding its way into the Computer Vision community.

References

- Albl C, Kukulova Z, Pajdla T (2015) R6P - Rolling Shutter Absolute Pose Problem. In: Proc. CVPR
- Albl C, Kukulova Z, Pajdla T (2016) Rolling shutter absolute pose problem with known vertical direction. In: Proc. CVPR
- Apple (2015) ARKit. <https://developer.apple.com/augmented-reality/>
- Bapat A, Price T, Frahm JM (2018) Rolling shutter and radial distortion are features for high frame rate multi-camera tracking. In: Proc. CVPR
- Campos C, Montiel J, Tardós J (2019) Fast and Robust Initialization for Visual-Inertial SLAM. In: Proc. ICRA
- Chojnacki W, Brooks MJ, van den Hengel A, Gawley D (2000) On the fitting of surfaces to data with covariances. PAMI 22(11)
- Chojnacki W, Brooks MJ, van den Hengel A (2001) Rationalising the renormalisation method of Kanatani. Journal of Mathematical Imaging and Vision 14:21–38
- Dai Y, Li H, Kneip L (2016) Rolling shutter camera relative pose: Generalized epipolar geometry. In: Proc. CVPR
- Dong-Si T, Mourikis AI (2012) Estimator initialization in vision-aided inertial navigation with unknown camera-imu calibration. In: IEEE/RSJ International Conference on Intelligent Robots and Systems
- Epic Games (2019) Unreal Engine. <http://www.unrealengine.com>
- Evangelidis G, Micusik B (2021) Revisiting visual-inertial structure-from-motion for odometry and SLAM initialization. Robotics and Automation Letters (RA-L) 6(2)
- Evangelidis GD, Psarakis EZ (2008) Parametric image alignment using enhanced correlation coefficient maximization. PAMI 30(10)
- Forster C, Carlone L, Dellaert F, Scaramuzza D (2017) On-manifold preintegration for real-time visual-inertial odometry. IEEE TRO 33(1)
- Förstner W, Wrobel B (2016) Photogrammetric Computer Vision. Springer
- Golub GH, van Loan CF (2013) Matrix Computations, 4th edn. JHU Press
- Google (2018) ARCore. <https://developers.google.com/ar>
- Gupta R, Hartley RI (1997) Linear pushbroom cameras. PAMI 19(9)
- Hartley RI, Zisserman A (2004) Multiple View Geometry in Computer Vision. Cambridge University Press
- Hedborg J, Forssen PE, Felsberg M, Ringaby E (2012) Rolling shutter bundle adjustment. In: Proc. CVPR
- Huang W, Liu H, Wan W (2020) An online initialization and self-calibration method for stereo visual-inertial odometry. TRO Preprint
- Kaiser J, Martinelli A, Fontana F, Scaramuzza D (2017) Simultaneous state initialization and gyroscope bias calibration in visual inertial aided navigation. IEEE Robotics and Automation Letters 2(1):18–25
- Kanatani K (1996) Statistical Optimization for Geometric Computation: Theory and Practice. Elsevier Science Inc., USA
- Kanatani K (2008) Statistical optimization for geometric fitting: Theoretical accuracy bound and high order error analysis. IJCV 80
- Kanatani K (2014) Statistical optimization for geometric estimation: Minimization vs. non-minimization. In: Proc. ICPR
- Kanatani K, Sugaya Y, Kanazawa Y (2016) Guide to 3D Vision Computation. Springer Verlag
- Kneip L, Weiss S, Siegwart R (2011) Deterministic initialization of metric state estimation filters for loosely-coupled monocular vision-inertial systems. In: IEEE/RSJ International Conference on Intelligent Robots and Systems
- Leedan Y, Meer P (2000) Heteroscedastic Regression in Computer Vision: Problems with Bilinear Constraint. IJCV 37(2)
- Li M, Kim B, Mourikis A (2013) Real-time motion tracking on a cellphone using inertial sensing and a rolling-shutter camera
- Ling Y, Bao L, Jie Z, Zhu F, Li Z, Tang S, Liu Y, Liu W, Zhang T (2018) Modeling varying camera-imu time

- offset in optimization-based visual-inertial odometry. In: Proc. ECCV
- Lourakis MLA, Argyros AA (2005) Is Levenberg-Marquardt the most efficient optimization algorithm for implementing bundle adjustment? In: Proc. ICCV, vol 2
- Martinelli A (2013) Closed-form solution of visual-inertial structure from motion. IJCV
- Meingast M, Geyer C, Sastry S (2005) Geometric models of rolling-shutter cameras. CoRR
- Mourikis AI, Roumeliotis SI (2007) A multi-state constraint kalman filter for vision-aided inertial navigation. In: Proc. ICRA
- Mur-Artal R, Tardós JD (2017) Visual-inertial monocular slam with map reuse. IEEE Robotics and Automation Letters 2(2)
- Mur-Artal R, Montiel J, Tardós JD (2015) ORB-SLAM: a versatile and accurate monocular slam system. TRO 31(5)
- Okatani T, Deguchi K (2009) On bias correction for geometric parameter estimation in computer vision. In: Proc. CVPR
- Patron-Perez A, Lovegrove S, Sibley G (2015) A spline-based trajectory representation for sensor fusion and rolling shutter cameras. IJCV 113
- Qin T, Shen S (2017) Robust initialization of monocular visual-inertial estimation on aerial robots. In: IEEE/RSJ International Conference on Intelligent Robots and Systems
- Rosten E, Porter R, Drummond T (2010) FASTER and better: A machine learning approach to corner detection. PAMI 32:105–119
- Schubert D, Demmel N, Usenko V, Stückler J, Cremers D (2018) Direct sparse odometry with rolling shutter. In: Proc. ECCV
- Schubert D, Demmel N, Stumberg L, Usenko V, Cremers D (2019) Rolling-shutter modelling for direct visual-inertial odometry
- Taubin G (1991) Estimation of planar curves, surfaces, and nonplanar space curves defined by implicit equations with applications to edge and range image segmentation. PAMI 13(11)